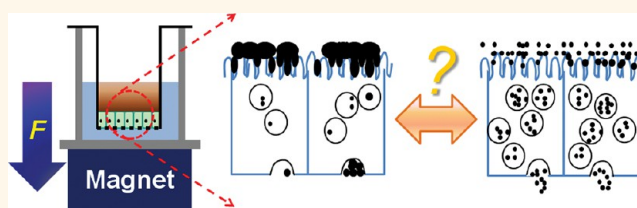


Pulsed Magnetic Field Improves the Transport of Iron Oxide Nanoparticles through Cell Barriers

Kyoung Ah Min,[†] Meong Cheol Shin,[†] Faquan Yu,[‡] Meizhu Yang,[‡] Allan E. David,[§] Victor C. Yang,^{†,⊥} and Gus R. Rosania^{†,*}

[†]Department of Pharmaceutical Sciences, College of Pharmacy, University of Michigan, Ann Arbor, Michigan 48109, United States, [‡]Key Laboratory for Green Chemical Process of Ministry of Education, Wuhan Institute of Technology, Wuhan 430073, China, [§]Department of Chemical Engineering, Auburn University, Auburn, Alabama 36849, United States, and [⊥]Tianjin Key Laboratory on Technologies Enabling Development of Clinical Therapeutics and Diagnosis, School of Pharmacy, Tianjin Medical University, Tianjin 300070, China

ABSTRACT Understanding how a magnetic field affects the interaction of magnetic nanoparticles (MNPs) with cells is fundamental to any potential downstream applications of MNPs as gene and drug delivery vehicles. Here, we present a quantitative analysis of how a pulsed magnetic field influences the manner in which MNPs interact with and penetrate across a cell monolayer. Relative to a



constant magnetic field, the rate of MNP uptake and transport across cell monolayers was enhanced by a pulsed magnetic field. MNP transport across cells was significantly inhibited at low temperature under both constant and pulsed magnetic field conditions, consistent with an active mechanism (*i.e.*, endocytosis) mediating MNP transport. Microscopic observations and biochemical analysis indicated that, in a constant magnetic field, transport of MNPs across the cells was inhibited due to the formation of large (>2 μm) magnetically induced MNP aggregates, which exceeded the size of endocytic vesicles. Thus, a pulsed magnetic field enhances the cellular uptake and transport of MNPs across cell barriers relative to a constant magnetic field by promoting accumulation while minimizing magnetically induced MNP aggregation at the cell surface.

KEYWORDS: magnetic field · superparamagnetic iron oxide nanoparticles · magnetic targeting · drug delivery · bioimaging · magnetically guided therapy · cell-based assays

Interest in magnetic nanoparticles (MNPs) has been considerably raised by their numerous biomedical applications, including cell labeling,¹ *in vitro* cell separation,^{2,3} drug/gene delivery,^{4,5} and contrast agents in magnetic resonance imaging (MRI).^{6,7} Magnetic guiding of MNPs, for example, could be very useful in tissue engineering by facilitating delivery of attached cargoes in a precise, spatially controlled manner. These applications are enabled by the unique physicochemical properties of MNPs, including intrinsic magnetic susceptibility,^{8,9} small particle sizes,^{10,11} and multifunctional surface chemistry.^{12,13} MNPs having an iron oxide core (magnetite (Fe_3O_4) or maghemite (Fe_2O_3)) and exhibiting superparamagnetic behavior, often referred to as superparamagnetic iron oxide nanoparticles (SPION) or magnetic iron oxide nanoparticles (MION), have attracted attention due to their relatively low toxicity profile. Their

superparamagnetic property insures particle stability under storage and use, while their responsiveness to applied magnetic fields can be exploited for magnetically guided particle targeting¹⁴ or imaging.¹⁵

The cellular targeting or transcellular transport of MNPs under the influence of a magnetic force can be differentially enhanced through various pathways.^{16,17} Previously, we observed that magnetic fields can promote apical-to-basolateral transport of heparin-coated MNPs across epithelial cell monolayers, but only at low particle concentrations.¹⁸ Interestingly, transport of MNPs was inhibited at higher particle concentrations. This may be due to the increased tendency of MNPs to form aggregates in suspension at higher concentrations.¹⁹ Nanoparticles composed of bare iron oxide cores are especially susceptible to aggregate formation by van der Waals attraction forces.²⁰ These attractive

* Address correspondence to grosania@umich.edu.

Received for review October 27, 2012 and accepted February 1, 2013.

Published online February 01, 2013
10.1021/nn3057565

© 2013 American Chemical Society

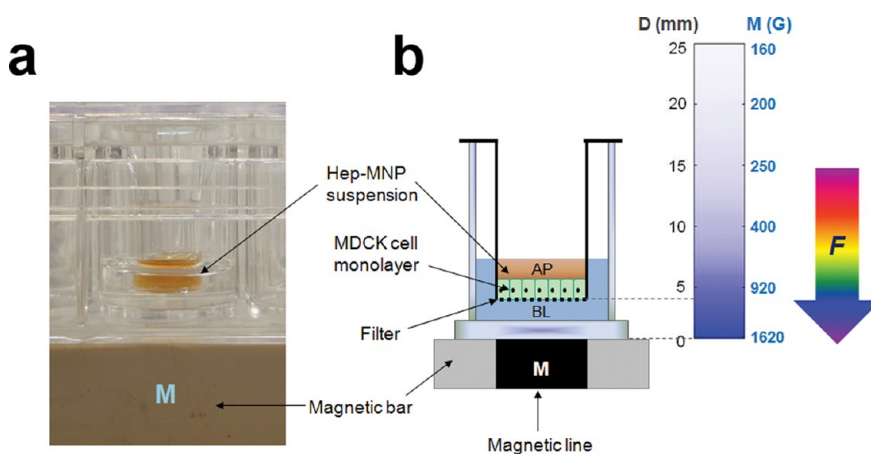


Figure 1. MNP transport experiments were carried out using Transwell inserts. (a) Experimental setup with the transport system using Transwell insert. Supported MDCK (Madin–Darby canine kidney) II cell monolayers were grown on porous polyester membrane and used for apical (AP)-to-basolateral (BL) transport studies with 24-well plate placed on a magnetic bar. Heparin-coated MNPs (Hep-MNPs) suspensions were loaded in the apical side. The transport of MNPs across cells was monitored by collecting samples from the basolateral side. (b) Schematic representation of the transport system with the magnetic flux density map. Dimensions of the experimental setting are depicted in mm units. Vertical color gradient bar represents the magnetic flux density (M , G) as a function of the distance from the surface of magnet (D , mm).

forces are often overcome through modification of the surface chemistry of MNPs.^{20–24} Surface modification can improve the stability of MNPs as drug carriers in physiological media,^{18,25} increase drug/gene targeting efficiency *in vivo*,²⁶ and facilitate the targeting of MNPs to tumor sites.^{27,28}

For individual particles, size,^{10,11,29} surface chemistry,^{12,13} and surface charge¹⁶ are key factors that affect particle interactions with cells. Nevertheless, even surface-modified MNPs may agglomerate and form large clusters under the influence of a magnetic field due to the induced magnetic dipole–dipole attractions.^{30,31} Effects of magnetic fields on the aggregation state of MNPs in the human body are largely unknown. However, animal studies indicate that magnetically induced MNP aggregation can affect the performance of MNPs in drug targeting and delivery applications.³² Furthermore, MNP aggregates can clog blood vessels and accumulate in off-target sites.^{33,34} Because of these known complications, understanding how an applied magnetic field affects the aggregation state of MNPs interacting with cells could be important and relevant for optimizing the behavior of MNPs as MRI contrast agents and as magnetically guided drug or gene delivery vehicles.

Here, we studied the effects of MNP aggregate formation on targeting and transport across a cell barrier. Using a controlled *in vitro* assay system to enable quantitative measurement of particle transport kinetics (Figure 1), we assessed the differential effects of a pulsed magnetic field and constant magnetic field on the transport of particles across the cell monolayer and their intracellular uptake and retention on the cell surface. In our experimental setup, MNPs were added in suspension to the apical (donor) compartment on top of a confluent epithelial cell monolayer

differentiated on a porous membrane support. A magnetic field was applied from the opposite side of the membrane and was either kept constant or pulsed on and off. Transport experiments were performed under different temperature conditions to determine the influence of active cellular processes on particle targeting, uptake, and transport. Finally, effects of spatiotemporal changes of the external magnetic field on the particle transport kinetics were investigated by transmission electron microscopy and confocal microscopy and related to bulk quantitative measurements of particle mass distribution.

RESULTS

Enhanced Cellular Uptake and Penetration under a Pulsed Magnetic Field. Visual inspection after transport studies under the constant magnetic field indicated a greater accumulation of microscopically visible MNP aggregates on the cell monolayers with increasing concentrations of MNP in the donor compartment (Figure S2 in the Supporting Information). Under constant magnetic field conditions, the area of the cell surface visibly covered by MNP aggregates at high MNP concentration (0.412 mg Fe/mL) was 34% (± 2.99), 3-fold larger than those at lower concentration (0.258 mg Fe/mL) (11% (± 5.00)) (Unpaired *t* test, *p* value = 0.0022). Thus, we hypothesized that the decrease in the rate of particle transport under constant magnetic field conditions at higher initial MNP concentration might be due to the increased retention of large, magnetically induced MNP aggregates at the cell surface. To test this possibility, we decided to determine whether a pulsed magnetic field could be used to promote transport across a cell barrier relative to a constant magnetic field condition by minimizing the formation of large magnetized aggregates while pulling the MNPs toward the

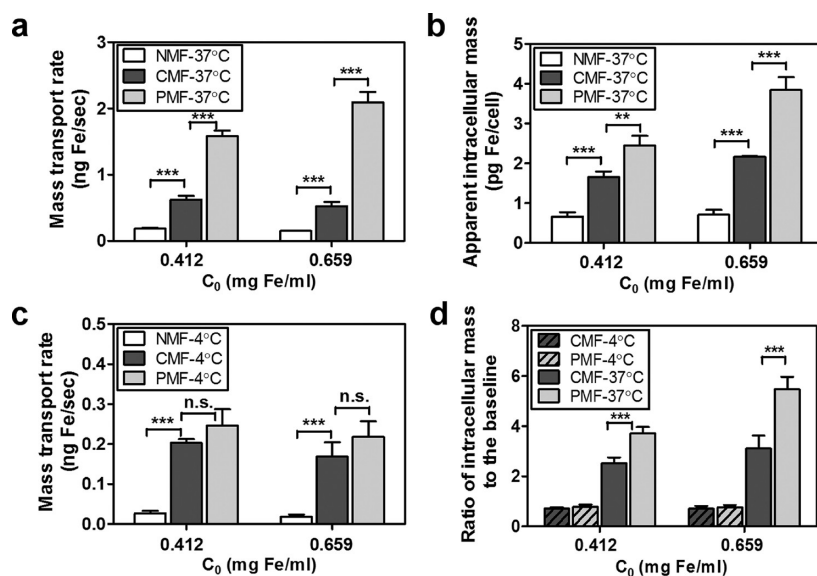


Figure 2. Mass transport of MNPs across MDCK cell monolayers was differentially affected by increasing MNP concentrations (0.412 or 0.659 mg Fe/mL) under various magnetic field conditions (NMF corresponds to “no magnetic field”; CMF means “constant magnetic field”; and PMF is “pulsed magnetic field”; $N = 3$). (a) Mass transport rates of MNPs and (b) apparent intracellular masses of MNPs per cell, after a 90 min transport experiment, for different initial MNP concentrations (C_0 : 0.412 or 0.659 mg Fe/mL) under various magnetic field conditions (NMF, CMF, or PMF; 37 °C). (c) Rates of mass transport of MNPs across cells at 4 °C, at 0.412 or 0.659 mg Fe/mL under different magnetic field conditions (NMF, CMF, or PMF). (d) Ratio of intracellular masses of MNPs divided by the baseline, intracellular mass measured under NMF condition at 37 °C, as calculated after 90 min transport experiments under various experimental conditions (4 vs 37 °C; CMF vs PMF). For statistical analysis, one-way ANOVA test was followed by Tukey's multiple comparison tests ($\alpha = 0.05$) to determine significant differences between the means.

cell surface and across the cells. To test this, the transport of particles across MDCK cell monolayers was assessed under pulsed magnetic field, constant magnetic field, or no magnetic field conditions (Figure 2). Under pulsed magnetic field conditions, at high MNP concentrations (0.412 and 0.659 mg Fe/mL), the rate of particle transport across cells increased 8.5- and 13.6-fold compared to the rate of transport under no magnetic field conditions, respectively (Figure 2a). Compared with constant magnetic field conditions, a 2.5-fold greater rate of particle transport across cells was observed under pulsed magnetic field conditions, at MNP concentration of 0.412 mg Fe/mL (Figure 2a). This enhancement in particle transport rate was even greater (4-fold) at the highest MNP concentration tested (0.659 mg Fe/mL; Figure 2a). A comparison of the mass of MNPs internalized by cells under various magnetic field conditions (Figure 2b) revealed the apparent intracellular mass was 1.5- to 1.8-fold higher under pulsed magnetic field than under constant magnetic field conditions, indicating that pulsing the magnet promoted both intracellular uptake and transport of MNPs.

Lowering Temperature Inhibited MNP Transport under a Magnetic Field. The rate of MNP transport across the cell monolayers and the intracellular accumulation of MNPs in the presence of a magnetic field were significantly lower at 4 °C relative to the corresponding rates measured in transport experiments done at 37 °C (Figure 2c). In fact, the intracellular uptake of MNPs was

reduced to the point that intracellular MNP mass at 4 °C under pulsed or constant magnetic field conditions was similar to the intracellular accumulation of MNPs measured in no magnetic field at 37 °C. At 37 °C, the intracellular masses of MNPs under pulsed and constant magnetic field conditions were 3.7- to 5.5-fold and 2.5- to 3.1-fold greater, depending on MNP concentration, than that observed under no magnetic field conditions, respectively (Figure 2d). However, when the studies were repeated under 4 °C, no significant increase in intracellular mass accumulation was found under pulsed or constant magnetic field relative to no magnetic field conditions (Figure 2d). Therefore, it was realized that lowering the temperature dramatically inhibited both the cellular uptake and transport of MNPs, even in the presence of the external magnetic field.

Decreased MNP Transport Were Associated with Increased MNP Accumulations on Cells. On the basis of mass balance analysis using eqs 1–5 in the Materials and Methods, the transported fraction of MNPs under a constant magnetic field condition (α) was decreased from 8% (± 0.72) to 4% (± 0.52) with increasing initial MNP concentrations (Figure 3a). However, the fraction of particles retained on the cell surface (δ) exhibited a corresponding increase with increasing starting MNP concentration from 25% (± 1.42) at 0.412 mg Fe/mL to 36% (± 6.31) at 0.659 mg Fe/mL (Figure 3b). Under pulsed magnetic field conditions, however, a significantly greater fraction of particles crossed the cell

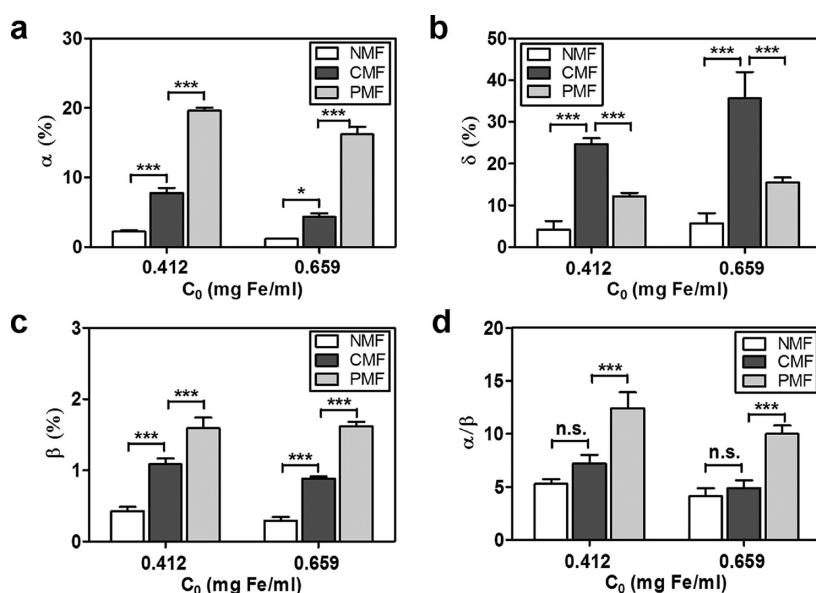


Figure 3. Mass balance analysis revealed different fractions of MNPs associated with different compartments, after transport experiments across cell monolayers under different magnetic field conditions. Transport experiments were done at 0.412 or 0.659 mg Fe/mL (C_0), and data were subjected to mass balance analysis (eqs 1–5). (a) Apical-to-basolateral transported fraction of MNPs, α (%); (b) fraction of particles bound to the cell surface, δ (%); (c) fraction of particles inside the cells, β (%). (d) Ratio (α/β) is depicted at 0.412 or 0.659 mg Fe/mL under various magnetic field conditions (NMF, CMF, or PMF). Statistical analysis was performed using one-way ANOVA with Tukey's multiple comparison tests ($\alpha = 0.05$) to determine significant differences between the means.

monolayer (α), while decreased particle masses were retained on the apical surface of the cells (δ), compared to results obtained with a constant magnetic field. Under a pulsed magnetic field condition, the fraction of intracellular particles (β) remained almost constant, from 1.59% (± 0.15) at 0.412 mg Fe/mL to 1.62% (± 0.06) at 0.659 mg Fe/mL, as the initial MNP concentration increased (Figure 3c). The differential effect of the magnet on the transport *versus* intracellular uptake of MNPs (α/β) was determined by calculating the ratio of the fraction of MNPs transported across the cells (α) divided by the fraction of particles trapped inside the cells (β). While there was no significant change of α/β under constant magnetic field compared to no magnetic field, notably, α/β increased about 2.5-fold under pulsed magnetic field relative to no magnetic field conditions (Figure 3d). Thus, while transport of MNPs across cellular barriers was enhanced over intracellular uptake under all conditions tested, the transport/uptake ratio was greatest under pulsed magnetic field conditions.

Cell Surface-Associated MNP Aggregates Formed faster than Uptake under a Constant Magnetic Field. In order to assess whether the large, visible particle aggregates that accumulated on the cell surface under constant magnetic field conditions formed in suspension prior to contacting the cells, we measured the aggregation behavior of MNPs in the absence of the supported cell monolayers, as a function of distance from the magnet. Experiments were performed by subjecting MNP suspension in a transparent glass tube to the same magnetic field conditions used in our Transwell insert setup. A microscope was used to image the formation

of MNP aggregates as a function of distance from the magnet over time, under 1000 \times magnification. At 0.412 mg Fe/mL (initial donor MNPs concentration), visible particle aggregates were detectable only at <0.5 mm from the magnet's surface (Figure S4a). After 30 min under the magnetic field, visible particle aggregates were observed between 1 and 2 mm from the magnet. However, at distances ≥ 3 mm from the magnet, no particle aggregates were visible microscopically, even after 3 h. For statistical analysis, the area of MNP clusters was measured in microscopic images (Figure 4a). Within the closest distance from the magnet (≤ 1 mm), massive aggregation was observed as early as 10 min in a constant magnetic field.

Nevertheless, as the distance from the magnet increased, the size of visible particle aggregates precipitously decreased. At distances ≥ 3 mm, there were no microscopically measurable particle aggregates. To determine the extent to which the magnetic field affected the concentration of MNPs at the level of the Transwell insert, we also measured the changes in MNP concentration in suspension over time as a function of distance from the magnet (Figure 4b). Rapid movement of MNPs close to the magnet resulted in an increase in local concentration near the magnet. However, particles located >4 mm from the magnet (at the level of the Transwell insert) moved more slowly toward the magnet, leading to a small but insignificant change in MNP concentration at distances >4 mm from the magnet. Therefore, the results suggested that it was at the level of the cell monolayer that the magnetic force was sufficient to pull down the MNPs

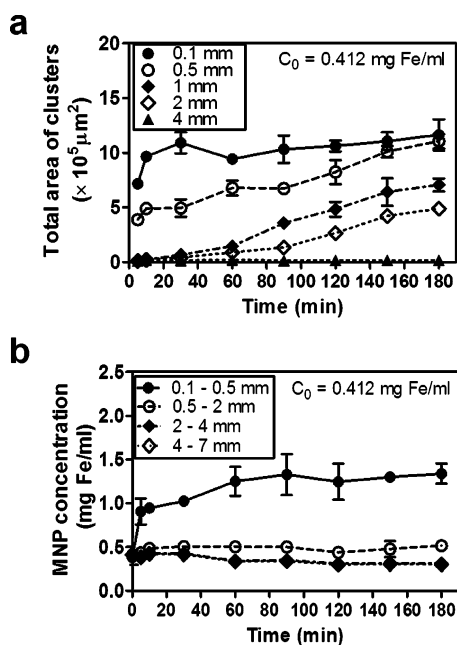


Figure 4. Visible, magnetically induced aggregation of MNPs in suspension decreased in size with increasing distance from the magnet. (a) Total sizes (area, μm^2) of clusters of particle aggregates measured from the bright-field images of particle suspension within 4 mm (0.1, 0.5, 1, 2, and 4 mm) from the magnet are displayed as a function of time (5–180 min) under the magnetic field. (b) MNP concentration changes at each segment in the tube (0.1–0.5, 0.5–2, 2–4, and 4–7 mm from the magnet) are plotted as a function of time (5–180 min) under the external magnetic field (0.412 mg Fe/mL).

onto the cell surface. The microscopically visible aggregates most likely formed after particles interacted with the surface of the cells. Although it is possible that some magnetically induced aggregates may be formed in suspension, those aggregates would have to be smaller than the resolution limit of the imaging system (<250 nm).

Magnetically Induced MNP Aggregation Did Not Affect Cellular Transport/Uptake in the Absence of Magnet. Control experiments were performed to determine whether inducing formation of MNP aggregates before adding them to the cells affected cell barrier penetration, cellular uptake, or retention on the cell surface when the transport experiments were carried out in the absence of a magnetic field. Mass transport rate and apparent intracellular mass of MNPs were measured, and for mass balance analysis, α , β , and δ (%) were calculated. Under these conditions, there were no significant differences in MNP transport, cellular uptake, and particle retentions on the cell surface in the absence of a magnetic field when MNP suspensions were exposed to different magnetic field conditions prior to the transport experiments (Figures S5 and S6). Cell images captured after the transport experiments did not reveal obvious differences in the accumulation of MNPs on the cell surface. These control experiments are consistent with the applied magnetic field mostly affecting the manner in which MNPs interact with the cells and with each

other at the moment they come in contact with the cell surface.

Pulsed Magnetic Field Enhanced Uptake/Transport and Decreased Cell Surface MNP Aggregates. To further investigate the pathway through which a pulsed magnetic field enhances transport of MNPs across cell monolayers relative to a constant magnetic field, cell monolayers were examined by TEM after 90 min transport experiments at 37°C . Under constant magnetic field conditions, large numbers of MNP aggregates were visible on the extracellular side of the apical cell surface at high MNP concentration (0.659 mg Fe/mL). The size of the particle aggregates on the cell surface was often $>2 \mu\text{m}$ (Figure 5a and zoom-in image). Smaller MNP aggregates were visible inside cells and were always observed inside the lumen of membrane-bound vesicles (Figure 5c). The intracellular aggregates were much smaller than those present on the extracellular face of the apical membrane (Figure 5b,c). Remarkably, under pulsed magnetic fields, the size of particle aggregates on the extracellular face of the apical membrane was 206 ± 125 nm, which was significantly smaller than the size of the aggregates measured under constant magnetic field conditions (551 ± 519 nm) (ANOVA, p value <0.001) (Figure 5d and zoom-in). Nevertheless, the intracellular MNP aggregates found inside membrane-bound vesicles in constant and pulsed magnetic field conditions were of similar size: 155 ± 123 and 140 ± 80 nm, respectively (Figure 5c,e,f). In the absence of magnetic field, there were fewer aggregates on the cell surface (Figure 5g, zoom-in, and h) than under the applied magnetic field. In negative control experiments, no particles were observed, as expected (Figure 5i). Thus, while intracellular MNP aggregates were always of size smaller than endosomes under various magnetic field conditions (Figure 5j), the size of MNP aggregates that formed under a constant magnetic field condition was greater than the size of the aggregates that fit in the endosomes, remaining on the extracellular, apical cell surface.

Large Particle Aggregates Formed at the Basolateral Side under a Constant Magnetic Field. Using optical microscopy, we also examined the transport of MNP suspension at high particle concentration (0.659 mg Fe/mL) across cell monolayers under different magnetic field conditions. Under bright-field illumination, there were visible differences in the accumulation of MNPs under various magnetic field conditions (Figure 6a). In the absence of magnetic field, no particle aggregates were detected by confocal epifluorescence microscopy (Figure 6b). Under constant magnetic field conditions, however, large MNP particle aggregates were observed not only on the apical side of the cells but also at the basolateral side of the cells, clogging the pores of the membrane. In contrast, under pulsed magnetic field conditions, although fluorescence of MNPs was

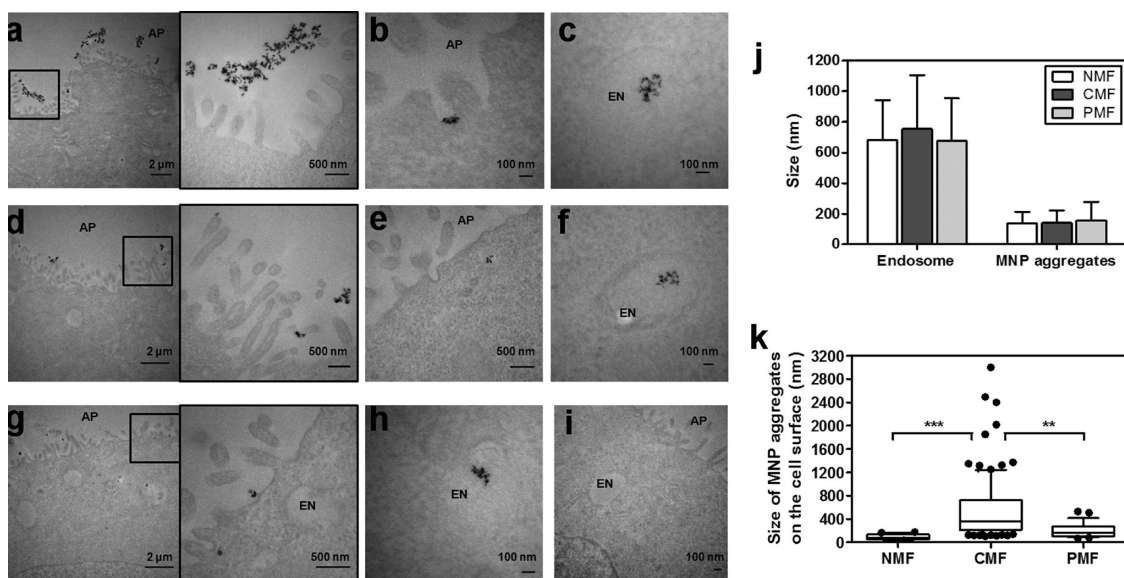


Figure 5. Transmission electron microscopy (TEM) revealed different sizes of MNP aggregates associated with cell monolayers after transport experiments under different magnetic field conditions. “AP” and “EN” indicate apical side and endosome, respectively. Under CMF conditions, (a) large aggregates were visible on the extracellular face of the apical cell membrane (zoom-in image next to the original image); (b) smaller MNP aggregates were sometimes visible in the cell surface invaginations; (c) smaller MNP aggregates were observed inside endosomes. Under PMF conditions, (d) MNP aggregates on the extracellular face of the apical cell membrane were smaller in size; (e) some MNPs were also observed in apical membrane invaginations; (f) intracellular MNPs were observed inside endosomes. Under NMF conditions, (g) only small MNP aggregates were visible on the extracellular face of the apical cell surface; (h) some small MNP aggregates were observed inside endosomes. (i) In the absence of MNPs, no MNPs were observed on the cell surface and inside the cells. (j) Sizes of endosome and MNP aggregates inside the endosome measured by Metamorph are depicted for different magnetic field conditions (NMF, CMF, or PMF). (k) Sizes of MNP aggregates retained on the apical cell surface are compared in different magnetic field conditions (NMF, CMF, or PMF). Whisker plots with 10–90% percentiles are depicted with the solid dots as outliers. For statistical analysis, one-way ANOVA test followed by Tukey’s multiple comparison testing was used ($\alpha = 0.05$) to determine significant differences between the means.

observed in association with the cells, there were no large aggregates present on either the apical or basolateral sides of the cells.

DISCUSSION

On the basis of this study, a pulsed magnetic field can be used to enhance the transport of MNPs into and across a cellular barrier (Figure 7). In contrast, when the magnetic field is held constant, large magnetized aggregates form at the cell surface, resulting in a greatly decreased fraction of particles being endocytosed by the cells or actively transported across the cellular barrier. Microscopically visible MNP aggregates that formed at the cell surface in the presence of a constant magnetic field were too large to be taken up by endocytosis, and they accumulated on the cell surface at a faster rate than they were endocytosed by the cells. Based on the finding that all intracellular MNPs were found inside membrane-bound vesicles and that the size of MNP aggregates that can be accommodated by these vesicles is limited to the size of the vesicles, these results suggest that a constant magnetic field is less efficient at promoting MNP transport because large magnetized MNP clusters do not penetrate across the cellular barrier, due to steric constraints inhibiting their uptake. Supporting this notion, we did not observe any MNPs in the

intercellular spaces at the level of the cell monolayer. We also observed a dramatic inhibitory effect of lowering temperature on the ability of magnetic fields to promote transport of MNPs across the cell monolayers, consistent with transport of MNPs across the cells occurring *via* temperature-sensitive endocytic uptake, followed by transcytosis. In control transport experiments carried out in the absence of a magnet, MNP suspensions pre-exposed to a magnetic field exhibited similar transport behaviors as MNP suspensions that had not been pre-exposed to a magnetic field (Figures S5 and S6).

Mechanistically, our results point to endocytic uptake as a key factor affecting the interaction between MNPs and cells, even in the presence of an external magnetic field. This is consistent with previous studies.^{11,35} Inhibition of endocytosis by lowering the temperature reduced cellular uptake and transport of MNPs. Unfortunately, probing the role of endocytosis on the targeting and transport of MNPs is very difficult *in vivo*, and only a few such studies on middle ear epithelium have been conducted.^{36,37} Nevertheless, our observations suggest that TEM analyses could be performed to study how a magnetic field facilitates the targeting, transport, and cellular uptake of MNPs *in vivo*. In our experiments, TEM revealed the formation of sub-micrometer-sized cell surface aggregates that

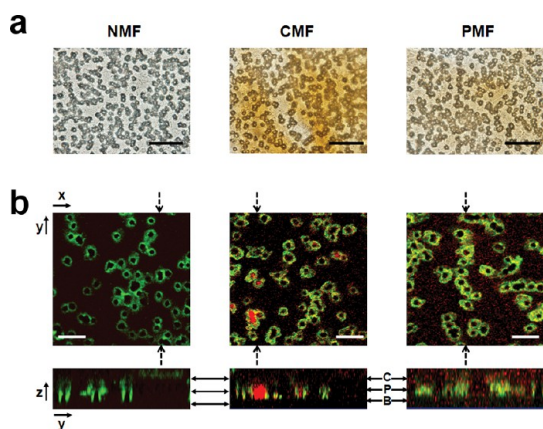


Figure 6. Transmitted light and confocal epifluorescence microscopy revealed MNP aggregates on cell monolayers and pores of the polyester membrane after 90 min transport studies with MNPs at high MNP concentration (0.659 mg Fe/mL). MNPs showed different aggregation patterns, depending on the magnetic field conditions (NMF, CMF, or PMF). (a) Images of supported cell monolayers captured by Olympus BX-51 upright light microscope under bright-field illumination at 1000 \times magnifications (scale bar = 10 μ m). (b) Images of TRITC-labeled MNPs acquired with a confocal fluorescence microscope, showing the pores of the membrane stained with LysoTracker Green dyes after 30 min incubation under NMF, CMF, or PMF conditions (scale bar = 10 μ m). The top image corresponds to a confocal plane across the PET membrane of the Transwell insert, parallel to the plane of the cell monolayer. The bottom image corresponds to an orthogonal yz plane cutting across the cells and the membrane, perpendicularly to the plane of the cell monolayer. Solid bidirectional arrows indicate cytoplasm (C), pore (P), and basolateral (B) side at each yz plane.

were endocytosed, as well as the formation of large, cell surface MNP aggregates that were not endocytosed. Functional differences in MNP performance could be correlated with the targeting and transport properties of MNPs, as well as size differences in MNP aggregates on the cell surface or basolateral membrane under the different magnetic field applications (constant vs pulsed magnetic field). Similar TEM observations could be performed *in vivo*.

For *in vitro* magnetic labeling or magnetofection applications, the quantitative analysis developed in this study can be used to reveal how the cellular uptake and targeting of particles are affected by the manner in which the external magnetic field is modulated. For *in vivo* drug targeting and delivery experiments, similar quantitative analysis of MNP aggregation and transport pathways will be essential to guide the future development of magnetic targeting strategies and their downstream application in drug or gene delivery. For clinical MRI, quantitative analyses of magnetic field-induced MNP aggregation could also help improve the performance of MNPs as contrast agents and prevent possible side effects that may result from induced particle aggregates (e.g., vascular thromboembolic events or unwanted accumulation of MNPs in off-target sites).^{32,34,38} While many physicochemical properties of MNP preparations can influence their

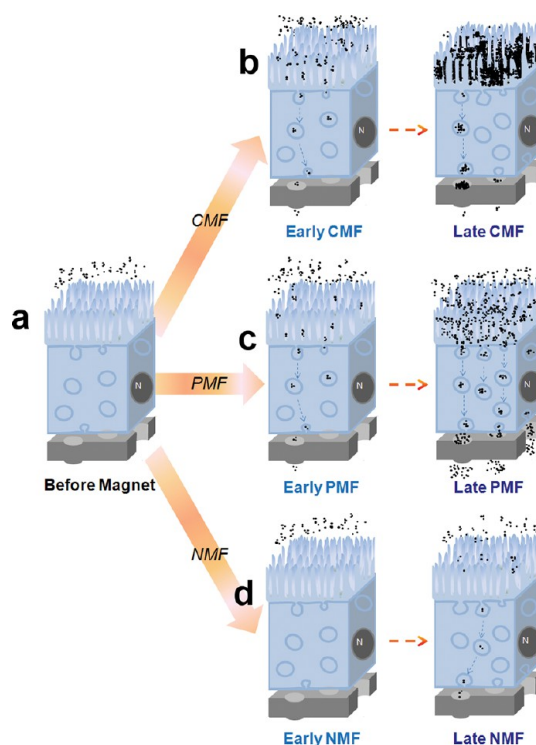


Figure 7. Descriptive diagram summarizing the different spatiotemporal behaviors of MNPs under various magnetic field conditions (NMF, CMF, or PMF) based on our quantitative and microscopic observations. “N” means cell nuclei. (a) Before the magnetic field is applied, most of MNPs (random assemblies of black dots) are suspended in the apical compartment. (b) Under CMF conditions, the suspended particles are attracted by the magnetic field toward the cell surface, translocated into the cell *via* endocytosis and to the basolateral side *via* transcytosis. At a later time point, accumulations of larger MNP aggregates on the cell surface sterically inhibit endocytosis of MNPs, and large MNP aggregates form on the basolateral side, clogging the pores on the membrane. (c) Under PMF conditions, translocation of the particles *via* endocytosis is facilitated by the pulsed magnetic field while the formation of particle aggregates on the cell surface is minimal. There is no clogging by MNP aggregates at the basolateral side of the cells. (d) In the absence of magnetic field (NMF), endocytic uptake of MNPs occurs slowly with much fewer MNP aggregates visible on the cell surface or in endocytic vesicles.

propensity to form aggregates,^{9,13,14} the performance of MNPs as contrast agents for MRI experiments can be affected by their magnetically induced aggregation state.³⁹ While magnetically induced MNP aggregates show decreased contrast enhancement in MRI,⁴⁰ our experiments are specifically relevant to MNP targeting in the context of magnetically guided therapy. Related to this, magnetic field strengths in clinical MRI instruments are orders of magnitude greater than those used in our transport experiments.^{32,41,42} Therefore, field-induced particle aggregates can be expected to form even more readily in clinical MRI applications.⁴³ Consistent with our experiments, continuous exposure to high strength magnetic fields does not necessarily lead to greater tissue targeting, as compared with lower strength magnetic fields.³²

Certainly, we expect that further quantitative analysis will be essential to identify MNP formulations with the most suitable physicochemical properties (*i.e.*, particle size, surface modifications, nanomaterial types, batch-to-batch variations) for *in vitro* and *in vivo* use and also clinical applications. Although our experiments did not test the performance of different MNP formulations, spatiotemporal variations in the magnetic field are expected to interact differently with MNP preparations possessing different physicochemical properties. Most likely, magnetic field strength, number, and frequency of pulses will need to be optimized in a formulation-specific manner, so as to achieve maximal uptake (or transfection efficiency). Perhaps, more importantly, our results clearly indicate the importance of exploring the effects of spatiotemporal variations in magnetic fields in the context of *in vivo* drug/gene delivery applications. Indeed, the vast majority of *in vivo* targeting/delivery and MRI experiments involving MNPs have been done in the presence of a constant magnetic field. While all our experiments have been done *in vitro*, our results suggest that the interaction of a pulsed magnetic field with particle dosing, the distance from the magnet, and overall duration of applying magnetic field may also be exploited to obtain the most effective, selective, and reliable magnetic applications. Previously, submaximal magnetic field strengths have been used *in vivo* to avoid severe particle aggregations that often occurs

during magnetic targeting experiments.⁴⁴ However, a pulsed magnetic field may offer distinct advantages in terms of its ability to minimize cell surface aggregate formation while maximizing the force driving the cellular uptake and transport of particles.

CONCLUSIONS

To summarize, the retention of MNPs on the cell surface, as well as the cellular uptake and transcellular targeting of MNPs, has been quantitatively analyzed in relation to the initial MNP concentrations and their interaction with a constant *versus* pulsed magnetic field. At high particle concentrations, the propensity of forming large particle aggregates after interaction of MNPs with the cell surface was reduced by pulsing on and off the magnetic field. Because of steric hindrance, large particle aggregates cannot be endocytosed, resulting in an increased fraction of MNPs accumulating at the cell surface when the magnetic field is kept constant. By pulsing the magnetic field, the apical to basolateral transport of MNPs across the cell monolayers was maximized by effectively concentrating MNPs at the cell surface while avoiding the formation of large MNP aggregates. Ultimately, our results suggest that spatiotemporal variations in the magnetic field can be effectively used to optimize *in vitro* and *in vivo* magnetically guided drug or gene targeting strategies for many potential clinically relevant applications.

MATERIALS AND METHODS

Materials. Chemicals used to prepare the Hep-MNPs or TRITC-labeled MNPs and quantify the iron contents (ferrozine assays) were obtained from the Sigma-Aldrich (St. Louis, MO). Chemicals used to prepare Hank's balanced salt solution buffer (HBSS; pH 7.4, 10 mM HEPES, 25 mM D-glucose) were from Fisher Scientific, Inc. (Pittsburgh, PA). Cell culture reagents and DYNAL-MPC-L magnet bar were purchased from Invitrogen (Carlsbad, CA). Transwell inserts with polyester membrane were purchased from Corning Co. (Lowell, MA). UV/vis plate reader (BioTEK Synergy BioTEK, Co.) was used to measure absorbance values of the samples from the transport experiments after ferrozine assays. A Phillips CM-100 transmission electron microscope and a Zeiss LSM 510-META laser scanning confocal microscope were used for cell examinations after transport experiments.

Preparation of Heparin-Coated Iron Oxide Nanoparticles (Hep-MNPs). As previously reported,¹⁸ a solution containing 0.76 mol/L of ferric chloride and 0.4 mol/L of ferrous chloride (molar ratio of ferric (Fe^{3+}) to ferrous (Fe^{2+}) = 2:1) was prepared at pH 1.7 under N_2 protection and then added into 1.5 M sodium hydroxide solution under stirring condition. The mixture was gradually heated (1 °C/min) to 78 °C and held at this temperature for 1 h with N_2 protection under stirring. After the supernatant was removed by a permanent magnet, the wet sol treated with 0.01 M HCl was sonicated for 1 h. The colloidal suspension of MNPs was filtered through a 0.45 μm and then a 0.22 μm membrane. Suspension was adjusted to contain 0.7 mg Fe/mL. Two hundred milliliters of 0.7 mg Fe/mL iron oxide nanoparticles was added to 200 mL of 1 mg/mL glycine with stirring. Next, the suspension was ultrasonicated for 20 min, followed by stirring for 2 h. After free glycine was removed by ultrafiltration, the iron content of the samples

was measured by inductively coupled plasma-optical emission spectroscopy (ICP) analysis using a Perkin-Elmer Optima 2000 DV instrument (Perkin-Elmer, Inc., Boston, MA), calibrated with an internal yttrium reference and a standard curve of iron samples (GFS Chemicals). The MNP suspension was diluted to a concentration of 0.35 mg Fe/mL. As a final step, 100 mL of 0.35 mg Fe/mL of glycine-MNPs was added to 100 mL of 1 mg/mL heparin solution, under stirring conditions and ultrasonication. Heparin-coated MNPs (Hep-MNPs) were obtained after free heparin was removed by ultrafiltration. Superparamagnetic properties of Hep-MNPs were confirmed with a superconducting quantum interference device (SQUID) (Quantum Design Inc., San Diego, CA, USA).¹⁸ Physicochemical characterization of MNP preparations was conducted by measuring the size and zeta-potential of MNPs in water or in the serum-containing buffer solution using Malvern Zetasizer (Malvern Instruments, Malvern, UK) (Figure S1).

Cell Culture. MDCK strain II cells obtained from American Type Culture Collection (ATCC) (Manassas, VA) were cultured in 75 cm^2 flasks at 37 °C, 5% CO_2 containing a humidified incubator. MDCK cells were cultured with growth medium consisting of Dulbecco's modified Eagle medium (DMEM; Invitrogen, Carlsbad, CA) with 2 mM L-glutamine, 4500 mg/L of D-glucose, and 110 mg/L of sodium pyruvate, 1 \times non-essential amino acids (Gibco 11140), 1% penicillin-streptomycin (Gibco 10378), and 10% fetal bovine serum (FBS; Gibco 10082). After reaching 70–80% confluency, MDCK cells were detached from the culture flasks using trypsin and subcultured at a split ratio of 1:10.

To prepare supported cell monolayers for transport experiments, cells in suspension (100 μL , 4×10^5 cells/ cm^2) were added into the apical side of Transwell inserts with the polyester (PET) membrane (area = 0.33 cm^2 , pore size = 3 μm) (Corning Co., Lowell, MA) in 24-well culture plate containing 600 μL of

growth media in the basolateral side. After overnight incubation at 37 °C, 5% CO₂ incubator, the confluent MDCK cell monolayers on Transwell inserts were rinsed twice with HBSS buffer (pH 7.4) and preincubated for 20 min in HBSS with 10% FBS (transport buffer) at 37 °C. Transepithelial electrical resistance of the cell monolayer was measured by Millipore Millicell ERS electrodes. TEER values were calculated after subtracting baseline TEER values measured with membrane inserts without cells. Only inserts with the confluent cells showing TEER values higher than 150 Ω × cm² were used for transport experiments.

Experimental Setup. Transport buffer (600 μL) without MNPs was added into the basolateral (bottom) chamber, and MNP suspension (100 μL of MNPs in transport buffer) at different initial concentrations was added to the apical (top) side of the Transwell insert. Apical-to-basolateral transport experiments were conducted over 90 min with or without the magnetic bar (DYNAL-MPC-L (Invitrogen, Carlsbad, CA)), applied to the bottom of the plate (Figure 1a). Magnetic flux density along the vertical distance from the surface of magnetic bar was measured by a 3-axis Hall Teslameter and depicted with color gradient map by the "TriScatteredInterp" function in MATLAB R2010b (Figure 1b).

Transport Measurements and Microscopic Imaging. During transport experiments, plates were stirred using a VWR rocking platform shaker. Sample solutions (300 μL) were collected from the basolateral chambers at each time point. Fresh 300 μL of transport buffer without the particles was then added back into the basolateral chambers. At the final time point (90 min), the solutions from donor and receiver chambers were collected, and both sides of the inserts were washed twice with cold Dulbecco's phosphate buffered saline (DPBS). For measurements, standard and sample solutions were put into the 96-well plates (Nalge Nunc International, Rochester, NY) for UV absorbance measurement at 364 nm using a plate reader (Synergy, BioTEK, Co.). Concentration of MNPs in the each well of the 96-well plate was determined with the aid of a standard curve.

To confirm monolayer integrity, TEER was measured after each experiment. Then, cell monolayers were washed with cold DPBS buffer, and the cells were examined using an Olympus BX-51 upright light microscope under bright-field illumination. Images of cell monolayers after experiments were acquired with an Olympus DP-70 digital camera. In the bright-field images, the clusters of particle aggregates in five different images at each case were analyzed by the integrated morphometric analysis (IMA) function of Metamorph (Molecular Devices, Inc.) (*N* = 5). Total clustered area of particle aggregates was normalized by overall cell monolayer and displayed as percentages for the comparisons at different initial MNP concentrations.

Effect of Magnetic Field Variations on Hep-MNP Transport. Transport studies under different conditions of the magnetic field were performed at 37 or 4 °C. For transport experiments in the presence of a constant magnetic field, the magnetic bar was fixed at the bottom of the plate and transport studies were performed for 90 min. For transport experiments under a pulsed magnetic field, cells were first incubated with MNPs but without the magnet during an initial 5 min period. Samples were taken out from basolateral side, after which the magnetic bar was placed at the bottom of the plate, and the MNP suspensions were incubated for an additional 5 min with shaking. At the end of the 5 min, the magnetic bar was removed and incubation was continued for 5 min more with shaking. In this manner, the magnetic field was pulsed for 8 cycles. Transport samples in the basolateral side were collected at 5, 10, 30, 50, and 70 min. At the final time point (90 min), the total volume was removed from apical and basolateral sides. To measure the intracellular content of MNPs, cells in the inserts were washed with cold DPBS buffer twice and detached from the membranes with trypsin. Trypsinization also removed the MNPs from the cell surface. The isolated cells were counted, and after centrifugation at 4000 rpm, 5 min, the cell pellets were lysed with 1% Triton X-100 (Sigma-Aldrich, St. Louis, MO) for 30 min on ice. After centrifugation at 12 000 rpm, 5 min, supernatants of the cell lysates were analyzed for iron content.

Quantitative Analysis of Iron Content. Iron content was measured using ferrozine-based assay. The solution of the Fe oxidizing agent, ferrozine, was prepared by solubilizing 80 mg of ferrozine, 68 mg of neocuproine, 9.635 g of ammonium acetate (final concentration = 5 M in solution), and 8.806 g of ascorbic acid (2 M in solution) in 25 mL of Milli-Q water (Bedford, MA) while stirring. For measurements, samples collected from transport studies were diluted in HBSS buffer. Diluted sample solution (83.3 μL) was mixed with 16.7 μL of 6 N HCl (final concentration of HCl in 100 μL solution is 1 N) in 1.5 mL microcentrifuge tubes. To release Fe from MNPs into solution, a potassium permanganate (KMnO₄) solution in HCl was prepared by mixing 3.55 mL of 0.2 M KMnO₄ with 1.5 mL of 2 M HCl. The sample solution (100 μL) was mixed with 100 μL of the KMnO₄/HCl solution and then heated in a 60 °C water bath for 2 h. Next, 30 μL of ferrozine solution was added to the samples and vortexed. The solution was cooled to room temperature and then 200 μL samples were transferred to a 96-well plate. Absorbance values were measured at 550 nm with UV/vis plate reader (BioTEK Synergy BioTEK, Co.). Iron standards were also prepared using the same procedure and subject to ICP. A standard curve was generated by ICP analysis and ferrozine assay using the Fe standard solutions in the range of Fe content (0–90 nmol Fe).

Quantitative Analysis of Mass Balance. For quantitative analysis of mass balance, transported fraction of MNPs (α , %), entrapped fraction of particles inside the cells (β , %), retained fraction of particles at apical suspension (γ , %), and retained fraction of particles at cell surface (δ , %) were calculated relative to the initial masses of MNPs (Map_initial) added to the cells at the start of each transport experiment, using eqs 1–5.

$$\alpha = \frac{Mbl_final}{Map_initial} \times 100 \quad (1)$$

$$\beta = \frac{IM_final}{Map_initial} \times 100 \quad (2)$$

$$\gamma = \frac{Map_final}{Map_initial} \times 100 \quad (3)$$

$$\delta = \frac{Mcellsurface}{Map_initial} \times 100 \quad (4)$$

$$Mcellsurface = Map_initial - Mbl_final - IM_final - Map_final - M_rinsed \quad (5)$$

In these equations, Mbl_final or Map_final refer to the mass of MNPs in basolateral (target) side or apical side at 90 min. IM_final refers to the measured intracellular mass of MNPs from the Triton-X-treated cells following removal of extracellular, cell-surface-associated MNPs by trypsin digestion. The masses of particles retained on the cell surface (Mcellsurface) were calculated by eq 5, corresponding to any residual particle masses that cannot be accounted for the masses in the intracellular, basolateral, or apical suspensions at 90 min and the masses in the solutions used to rinse the apical cell surface and basolateral side (M_rinsed). The ratio α/β was calculated from the fraction of targeted nanoparticles into the basolateral side over time (90 min) (α) normalized by the entrapped fraction of MNPs in the cells (β) at each case.

Transmission Electron Microscopy (TEM). Under different magnetic field conditions (no magnetic field, constant, or pulsed magnetic field), transport experiments in MDCK cell monolayers with MNPs at high particle concentration (0.659 mg Fe/mL) were performed at 37 °C, and then cells were prepared for TEM imagings. Cell monolayers on the inserts were washed twice with HBSS containing 10% FBS and then washed twice with Sorensen's buffer. The washed cells on inserts were fixed for 30 min with 2.5% glutaraldehyde in 0.1 M Sorensen's buffer (pH 7.4), followed by rinsing with 0.1 M Sorensen's buffer. Then, samples were incubated with 1% osmium tetroxide in 0.1 M Sorensen's buffer and rinsed twice with water. Next, samples were dehydrated for 5 min each in 50, 70, 90, and 100% ethanol,

infiltrated in Epon, and polymerized at 60 °C for 24 h. Embedded samples were sectioned with an ultramicrotome, and images were captured using a Phillips CM-100 transmission electron microscope at magnifications from 3400 to 180 000 \times . Images of MNP aggregates on the apical cell surface and cytosol were displayed with the scale bars. For the quantitative analyses of the TEM images, the diameter of the major axis in the elliptical circle of the endosome and the size of MNP aggregates were measured by Metamorph from at least 10 images under different magnetic field conditions. The sizes of endosome and MNP aggregates inside the endosome were measured by Metamorph from at least 10 different TEM images at each case of the applied magnetic field condition. In the case of endosome, the diameter in major axis of the endosome (assumed as an elliptical circle) was measured as the sizes of endosomes. The distance between both ends of the aggregates was measured as the size of MNP aggregates.

Confocal Microscopy. To examine the MNPs transported through the cells and pores in the membrane, Z-stack images were acquired using a Zeiss LSM 510-META laser scanning confocal microscope. For this purpose, Hep-MNPs labeled with TRITC were prepared. Rhodamine isothiocyanate (1 mg) (TRITC, Sigma-Aldrich) dissolved in 200 μ L of DMSO was slowly added to 5 mg of Fe (200 μ L of 25 mg Fe/mL stock solution) of Hep-MNPs. After incubation for 3 h at 25 °C, the reaction mixture was dialyzed (Sigma, MWCO = 12 kDa) against 10% DMF solution overnight with change of the dialyzing solution at every 6–8 h. Next, the reaction mixture was dialyzed against Milli-Q water. After transport studies with TRITC-labeled Hep-MNPs for 90 min with the applied magnetic field or without the applied magnetic field, the cells in the inserts were incubated with LysoTracker Green DND-26 (Molecular Probes, Invitrogen) for 30 min and then placed on the Lab-Tek I-chamber slide for live cell imaging. Particles were visualized in confocal scanning through Z-axis with a helium–neon 1 laser (543 nm).

Quantitative Microscopic Image Analysis of Magnet-Induced MNP Aggregates in Suspension. Ten microliters of MNP suspension in HBSS with 10% FBS was placed on a slide, and a no. 1 coverslip was placed on the drop of MNP suspension. The magnet was placed at the edge of the slide glass, and the particle aggregation of MNPs in the presence of magnetic field was measured over time (0–3 h) at varying distances from the magnet (0.1–10 mm) using an Olympus BX-51 upright light microscope at 1000 \times magnification. Using bright-field optics, images were captured with an Olympus DP-70 high-resolution digital camera at each time point (0, 5, 10, 30 min, and every 30 min until 3 h). After background subtraction and thresholding, the images were analyzed with Metamorph software (Molecular Devices, Inc.) using the IMA function to measure the area of clusters (particle aggregates). Total sizes (area, μ m²) of clusters of particle aggregates in the bright-field images of particle suspension within 2 mm (0.1, 0.5, 1, and 2 mm) from the magnet were measured by Metamorph for different initial MNP concentrations (0.258 or 0.412 mg Fe/mL).

Quantitative Analysis of Magnet-Induced Changes in MNP Concentration in Suspension. Over time, magnet-induced changes in MNP concentration were measured as a function of distance from the magnet, using a 1 mm diameter glass tube was filled with MNP suspension (0.258 or 0.412 mg Fe/mL) up to 20 mm along the tube. The magnetic bar was placed at the edge of the tube, horizontally, so the particles in suspension were pulled toward the magnet. Movement of MNPs toward the magnet to the distance from the magnet was examined using an UVP transilluminator (Upland, CA). Images of the tube aligned with the magnetic bar on the bright-field illuminator were captured using a Sony DSC-W70 digital camera (0–3 h). Intensity of the solution in the tube was measured using the line scan function in Metamorph from three different images. In the eq 6, I_0 or I_T indicates intensity of the solution in the tube at zero or each time point.

$$OD = \log \frac{I_0}{I_T} \quad (6)$$

On the basis of the optical density (OD), the mass of MNPs at each point along the tube was calculated with a standard curve

generated with the same setup, using MNP suspensions of known dilutions. Concentrations of MNPs at each segment in the tube (0.1–0.5, 0.5–2, 2–4, and 4–7 mm from the magnet) were calculated by dividing the integrated mass of MNPs over a length of the tube by the calculated volume of that segment of the tube, assuming a cylinder. Concentrations of MNPs (mg Fe/mL) moving toward the magnet across the tube were tracked with the time under the external magnetic field.

Statistical Analysis. GraphPad Prism 5.03 (GraphPad Software; LaJolla, CA) was used for data analyses. Unpaired Student's *t* test was used with a significance level of 0.05. As a post-test of one-way analysis of variance (one-way ANOVA), Tukey's multiple comparison test was performed with a significance level, $\alpha = 0.05$.

Conflict of Interest: The authors declare no competing financial interest.

Acknowledgment. This work was made possible through grants from NIH (R01GM078200 to G.R.R. and R01CA114612, R01NS066945 to V.C.Y.); NSF (EPS-1158862 Subagreement 34-21530-200-76190 to A.E.D.); World Class University (WCU) project of the MEST and NRF of South Korea (R31-2008-000-10103-01 to V.C.Y.); Warner Lambert/Parke Davis Fellowship (to K.A.M.); and a Rackham Predoctoral Fellowship of the University of Michigan (to K.A.M.). Authors thank A. Talattof for technical support, D. Sorenson (Microscopy and Image Analysis Laboratory, University of Michigan) for TEM analysis, and C. J. Galban (Department of Radiology, Center for Molecular Imaging, Medical School, University of Michigan) for helpful advice. V.C.Y. is also a Participating Faculty in the Department of Molecular Medicine and Biopharmaceutical Sciences, College of Medicine & College of Pharmacy, Seoul National University, South Korea.

Supporting Information Available: Additional experimental methods and results (figures). This material is available free of charge via the Internet at <http://pubs.acs.org>.

REFERENCES AND NOTES

- Ferrari, M. Cancer Nanotechnology: Opportunities and Challenges. *Nat. Rev. Cancer* **2005**, *5*, 161–171.
- Medarova, Z.; Pham, W.; Farrar, C.; Petkova, V.; Moore, A. *In Vivo* Imaging of siRNA Delivery and Silencing in Tumors. *Nat. Med.* **2007**, *13*, 372–377.
- Liong, M.; Lu, J.; Kovochich, M.; Xia, T.; Ruehm, S. G.; Nel, A. E.; Tamanoi, F.; Zink, J. I. Multifunctional Inorganic Nanoparticles for Imaging, Targeting, and Drug Delivery. *ACS Nano* **2008**, *2*, 889–896.
- Cheng, J.; Teply, B. A.; Jeong, S. Y.; Yim, C. H.; Ho, D.; Sherifi, I.; Jon, S.; Farokhzad, O. C.; Khademhosseini, A.; Langer, R. S. Magnetically Responsive Polymeric Microparticles for Oral Delivery of Protein Drugs. *Pharm. Res.* **2006**, *23*, 557–564.
- Dobson, J. Gene Therapy Progress and Prospects: Magnetic Nanoparticle-Based Gene Delivery. *Gene Ther.* **2006**, *13*, 283–287.
- Bulte, J. W. M. Magnetic Nanoparticles as Markers for Cellular MR Imaging. *J. Magn. Magn. Mater.* **2005**, *289*, 423–427.
- Peng, X. H.; Qian, X. M.; Mao, H.; Wang, A. Y.; Chen, Z.; Nie, S. M.; Shin, D. M. Targeted Magnetic Iron Oxide Nanoparticles for Tumor Imaging and Therapy. *Int. J. Nanomed.* **2008**, *3*, 311–321.
- Lu, A. H.; Salabas, E. L.; Schuth, F. Magnetic Nanoparticles: Synthesis, Protection, Functionalization, and Application. *Angew. Chem., Int. Ed.* **2007**, *46*, 1222–1244.
- Chatterjee, J.; Haik, Y.; Chen, C.-J. Size Dependent Magnetic Properties of Iron Oxide Nanoparticles. *J. Magn. Magn. Mater.* **2003**, *257*, 113–118.
- Muller, K.; Skepper, J. N.; Posfai, M.; Trivedi, R.; Howarth, S.; Corot, C.; Lancelot, E.; Thompson, P. W.; Brown, A. P.; Gillard, J. H. Effect of Ultrasmall Superparamagnetic Iron Oxide Nanoparticles (Ferumoxtran-10) on Human Monocyte-Macrophages *In Vitro*. *Biomaterials* **2007**, *28*, 1629–1642.

11. Chithrani, B. D.; Ghazani, A. A.; Chan, W. C. W. Determining the Size and Shape Dependence of Gold Nanoparticle Uptake into Mammalian Cells. *Nano Lett.* **2006**, *6*, 662–668.
12. Eberbeck, D.; Kettering, M.; Bergemann, C.; Zirpel, P.; Hilger, I.; Trahms, L. Quantification of the Aggregation of Magnetic Nanoparticles with Different Polymeric Coatings in Cell Culture Medium. *J. Phys. D: Appl. Phys.* **2010**, *43*.
13. Yuan, J. J.; Armes, S. P.; Takabayashi, Y.; Prassides, K.; Leite, C. A. P.; Galembek, F.; Lewis, A. L. Synthesis of Biocompatible Poly[2-(methacryloyloxy)ethyl phosphorylcholine]-Coated Magnetite Nanoparticles. *Langmuir* **2006**, *22*, 10989–10993.
14. Sonvico, F.; Mornet, S.; Vasseur, S.; Dubernet, C.; Jaillard, D.; Degrouard, J.; Hoebeke, J.; Duguet, E.; Colombo, P.; Couvreur, P. Folate-Conjugated Iron Oxide Nanoparticles for Solid Tumor Targeting as Potential Specific Magnetic Hyperthermia Mediators: Synthesis, Physicochemical Characterization, and *In Vitro* Experiments. *Bioconjugate Chem.* **2005**, *16*, 1181–1188.
15. Janib, S. M.; Moses, A. S.; MacKay, J. A. Imaging and Drug Delivery Using Theranostic Nanoparticles. *Adv. Drug Delivery Rev.* **2010**, *62*, 1052–1063.
16. Win, K. Y.; Feng, S. S. Effects of Particle Size and Surface Coating on Cellular Uptake of Polymeric Nanoparticles for Oral Delivery of Anticancer Drugs. *Biomaterials* **2005**, *26*, 2713–2722.
17. Yamamoto, H.; Kuno, Y.; Sugimoto, S.; Takeuchi, H.; Kawashima, Y. Surface-Modified PLGA Nanosphere with Chitosan Improved Pulmonary Delivery of Calcitonin by Mucoadhesion and Opening of the Intercellular Tight Junctions. *J. Controlled Release* **2005**, *102*, 373–381.
18. Min, K. A.; Yu, F.; Yang, V. C.; Zhang, X.; Rosania, G. R. Transcellular Transport of Heparin-Coated Magnetic Iron Oxide Nanoparticles (Hep-MION) under the Influence of an Applied Magnetic Field. *Pharmaceutics* **2010**, *2*, 119–135.
19. Koch, A. M.; Reynolds, F.; Merkle, H. R.; Weissleder, R.; Josephson, L. Transport of Surface-Modified Nanoparticles through Cell Monolayers. *ChemBioChem* **2005**, *6*, 337–345.
20. Petri-Fink, A.; Steitz, B.; Finka, A.; Salaklang, J.; Hofmann, H. Effect of Cell Media on Polymer Coated Superparamagnetic Iron Oxide Nanoparticles (SPIONs): Colloidal Stability, Cytotoxicity, and Cellular Uptake Studies. *Eur. J. Pharm. Biopharm.* **2008**, *68*, 129–137.
21. Kim, D. K.; Mikhaylova, M.; Zhang, Y.; Muhammed, M. Protective Coating of Superparamagnetic Iron Oxide Nanoparticles. *Chem. Mater.* **2003**, *15*, 1617–1627.
22. Zhang, L.; Yu, F. Q.; Cole, A. J.; Chertok, B.; David, A. E.; Wang, J. K.; Yang, V. C. Gum Arabic-Coated Magnetic Nanoparticles for Potential Application in Simultaneous Magnetic Targeting and Tumor Imaging. *AAPS J.* **2009**, *11*, 693–699.
23. Thunemann, A. F.; Schutt, D.; Kaufner, L.; Pison, U.; Mohwald, H. Maghemite Nanoparticles Protectively Coated with Poly(ethylene imine) and Poly(ethylene oxide)-Block-Poly(glutamic acid). *Langmuir* **2006**, *22*, 2351–2357.
24. Dias, A. M. G. C.; Hussain, A.; Marcos, A. S.; Roque, A. C. A. A Biotechnological Perspective on the Application of Iron Oxide Magnetic Colloids Modified with Polysaccharides. *Biotechnol. Adv.* **2011**, *29*, 142–155.
25. Wu, W.; He, Q.; Jiang, C. Magnetic Iron Oxide Nanoparticles: Synthesis and Surface Functionalization Strategies. *Nanoscale Res. Lett.* **2008**, *3*, 397–415.
26. Cole, A. J.; David, A. E.; Wang, J.; Galban, C. J.; Yang, V. C. Magnetic Brain Tumor Targeting and Biodistribution of Long-Circulating PEG-Modified, Cross-Linked Starch-Coated Iron Oxide Nanoparticles. *Biomaterials* **2011**, *32*, 6291–6301.
27. Chertok, B.; David, A. E.; Moffat, B. A.; Yang, V. C. Substantiating *In Vivo* Magnetic Brain Tumor Targeting of Cationic Iron Oxide Nanocarriers via Adsorptive Surface Masking. *Biomaterials* **2009**, *30*, 6780–6787.
28. Cole, A. J.; Yang, V. C.; David, A. E. Cancer Theranostics: The Rise of Targeted Magnetic Nanoparticles. *Trends Biotechnol.* **2011**, *29*, 323–332.
29. Huang, J.; Bu, L.; Xie, J.; Chen, K.; Cheng, Z.; Li, X.; Chen, X. Effects of Nanoparticle Size on Cellular Uptake and Liver MRI with Polyvinylpyrrolidone-Coated Iron Oxide Nanoparticles. *ACS Nano* **2010**, *4*, 7151–7160.
30. Socoliuc, V.; Taculescu, A.; Podaru, C.; Dobra, A.; Daia, C.; Marinica, O.; Turcu, R.; Vekas, L. Clustering in Water Based Magnetic Nanofluids: Investigations by Light Scattering Methods. *AIP Conf. Proc.* **2010**, *1311*, 89–95.
31. Espurz, A.; Alameda, J. M.; Espurznieta, A. Magnetically Induced Dielectric Anisotropy in Concentrated Ferrofluids. *J. Phys. D: Appl. Phys.* **1989**, *22*, 1174–1178.
32. Chertok, B.; David, A. E.; Yang, V. C. Brain Tumor Targeting of Magnetic Nanoparticles for Potential Drug Delivery: Effect of Administration Route and Magnetic Field Topography. *J. Controlled Release* **2011**, *155*, 393–399.
33. Driscoll, C. F.; Morris, R. M.; Senyei, A. E.; Widder, K. J.; Heller, G. S. Magnetic Targeting of Microspheres in Blood Flow. *Microvasc. Res.* **1984**, *27*, 353–369.
34. Duran, J. D.; Arias, J. L.; Gallardo, V.; Delgado, A. V. Magnetic Colloids as Drug Vehicles. *J. Pharm. Sci.* **2008**, *97*, 2948–2983.
35. Kim, J. S.; Yoon, T. J.; Yu, K. N.; Noh, M. S.; Woo, M.; Kim, B. G.; Lee, K. H.; Sohn, B. H.; Park, S. B.; Lee, J. K.; *et al.* Cellular Uptake of Magnetic Nanoparticle Is Mediated through Energy-Dependent Endocytosis in A549 Cells. *J. Vet. Sci.* **2006**, *7*, 321–326.
36. Mondalek, F.; Zhang, Y.; Kropp, B.; Kopke, R.; Ge, X.; Jackson, R.; Dormer, K. The Permeability of SPION over an Artificial Three-Layer Membrane Is Enhanced by External Magnetic Field. *J. Nanobiotechnol.* **2006**, *4*, 1–9.
37. Dormer, K.; Seeney, C.; Lewelling, K.; Lian, G.; Gibson, D.; Johnson, M. Epithelial Internalization of Superparamagnetic Nanoparticles and Response to External Magnetic Field. *Biomaterials* **2005**, *26*, 2061–2072.
38. Arruebo, M.; Fernández-Pacheco, R.; Ibarra, M. R.; Santamaria, J. Magnetic Nanoparticles for Drug Delivery. *Nano Today* **2007**, *2*, 22–32.
39. Tromsdorf, U. I.; Bigall, N. C.; Kaul, M. G.; Bruns, O. T.; Nikolic, M. S.; Mollwitz, B.; Sperling, R. A.; Reimer, R.; Hohenberg, H.; Parak, W. J.; *et al.* Size and Surface Effects on the MRI Relaxivity of Manganese Ferrite Nanoparticle Contrast Agents. *Nano Lett.* **2007**, *7*, 2422–2427.
40. Muller, R. N.; Gillis, P.; Mooney, F.; Roch, A. Transverse Relaxivity of Particulate MRI Contrast Media: From Theories to Experiments. *Magn. Reson. Med.* **1991**, *22*, 178–182.
41. Hartwig, V.; Giovannetti, G.; Vanello, N.; Lombardi, M.; Landini, L.; Simi, S. Biological Effects and Safety in Magnetic Resonance Imaging: A Review. *Int. J. Environ. Res. Public Health* **2009**, *6*, 1778–1798.
42. Riches, S. F.; Collins, D. J.; Scuffham, J. W.; Leach, M. O. Eu Directive 2004/40: Field Measurements of a 1.5 T Clinical MR Scanner. *Br. J. Radiol.* **2007**, *80*, 483–487.
43. David, A. E.; Cole, A. J.; Chertok, B.; Park, Y. S.; Yang, V. C. A Combined Theoretical and *In Vitro* Modeling Approach for Predicting the Magnetic Capture and Retention of Magnetic Nanoparticles *In Vivo*. *J. Controlled Release* **2011**, *152*, 67–75.
44. Gao, X.; Wang, Y.; Chen, K.; Grady, B. P.; Dormer, K. J.; Kopke, R. D. Magnetic Assisted Transport of PLGA Nanoparticles through a Human Round Window Membrane Model. *J. Nanotechnol. Eng. Med.* **2010**, *1*, 031010:1–6.